Available online at www.sciencedirect.com
SCIENCE DIRECT®
Journal of Computational Physics 213 (2006) 264–287
JOURNAL OF COMPUTATIONAL PHYSICS
www.elsevier.com/locate/jcp

Patch dynamics with buffers for homogenization problems

Giovanni Samaey [a,*], Ioannis G. Kevrekidis [b], Dirk Roose [a]

[a] Department of Computer Science, Katholieke Universiteit Leuven, Celestijnenlaan 200A, 3001 Leuven, Belgium
[b] Department of Chemical Engineering and PACM, Princeton University, Princeton, NJ 08544, USA

Received 29 November 2004; received in revised form 11 August 2005; accepted 11 August 2005
Available online 29 September 2005

Abstract

An important class of problems exhibits smooth behaviour on macroscopic space and time scales, while only a microscopic evolution law is known. For such time-dependent multi-scale problems, an "equation-free" framework has been proposed, of which patch dynamics is an essential component. Patch dynamics is designed to perform numerical simulations of an unavailable macroscopic equation on macroscopic time and length scales; it uses appropriately initialized simulations of the available microscopic model in a number of small boxes (patches), which cover only a fraction of the space-time domain. We show that it is possible to use arbitrary boundary conditions for these patches, provided that suitably large buffer regions "shield" the boundary artefacts from the interior of the patches. We analyze the accuracy of this scheme for a diffusion homogenization problem with periodic heterogeneity and illustrate the approach with a set of numerical examples, which include a non-linear reaction–diffusion equation and the Kuramoto–Sivashinsky equation.

Keywords: Multi-scale computation; Equation-free methods; Patch dynamics; Gap-tooth scheme; Homogenization

1. Introduction

For an important class of multi-scale problems, a separation of scales prevails between the (microscopic, detailed) level of description of the available model, and the (macroscopic, continuum) level at which one would like to observe and analyze the system. Consider, for example, a kinetic Monte-Carlo model of bacterial growth [37]. A stochastic model describes the probability of an individual bacterium to run or "tumble", based on the rotation of its flagellae. Technically, it would be possible to simply evolve the detailed

* Corresponding author. Tel.: +32 16 327082; fax: +32 16 327996.
E-mail addresses: giovanni.samaey@cs.kuleuven.ac.be (G. Samaey), yannis@princeton.edu (I.G. Kevrekidis), dirk.roose@cs.kuleuven.ac.be (D. Roose).

0021-9991/$ - see front matter © 2005 Elsevier Inc. All rights reserved.
doi:10.1016/j.jcp.2005.08.010

model and observe the macroscopic variables of interest (e.g. cell density), but this could be prohibitively expensive. It is known, however, that, under certain conditions, one could write a deterministic equation for the evolution of the macroscopic observable (here *bacteria concentration*, the zeroth moment of the evolving distribution) on macroscopic space and time scales, but it is hard to obtain an accurate closed formula explicitly.

The recently proposed *equation-free framework* [25] can then be used instead of stochastic time integration in the entire space-time domain. This framework is built around the central idea of a *coarse time-stepper*, which is a time-δt map from coarse variables to coarse variables. It consists of the following steps: (1) *lifting*, i.e., the creation of *appropriate* initial conditions for the microscopic model; (2) *evolution*, using the microscopic model and (possibly) some constraints; and (3) *restriction*, i.e., the projection of the detailed solution to the macroscopic observation variables. This coarse time-stepper can subsequently be used as "input" for time-stepper based algorithms performing macroscopic numerical analysis tasks. These include, for example, time-stepper based bifurcation codes to perform bifurcation analysis for the *unavailable* macroscopic equation [29,30,41,42]. This approach has already been used in several applications [21,39], and also allows to perform other system level tasks, such as control and optimization [38].

When dealing with systems that would be described by (in our case, unavailable) *partial* differential equations (PDEs), one can also reduce the spatial complexity. For systems with one space dimension, the *gap-tooth scheme* [25] was proposed; it can be generalized in several space dimensions. A number of small intervals, separated by large gaps, are introduced; they qualitatively correspond to mesh points for a traditional, continuum solution of the unavailable equation. In higher space dimensions, these intervals would become *boxes* around the coarse mesh points, a term that we will also use throughout this paper. We construct a coarse time-δt map as follows. We first choose a number of macroscopic grid points. Then, we choose a small interval around each grid point; initialize the fine scale, microscopic solver within each interval consistently with the macroscopic initial condition profiles; and provide each box with appropriate boundary conditions. Subsequently, we use the microscopic model in each interval to simulate until time δt, and obtain macroscopic information (e.g. by computing the average density in each box) at time δt. This amounts to a coarse time-δt map; the procedure is then repeated. The resulting scheme has already been used with lattice–Boltzmann simulations of the Fitzhugh–Nagumo dynamics [24,25] and with particle-based simulations of the viscous Burgers equation [15].

To increase the efficiency of time integration, one can use the gap-tooth scheme in conjunction with any method-of-lines time integration method, such as projective integration [13]. We then perform a number of gap-tooth steps of size δt to obtain an estimate of the time derivative of the unavailable macroscopic equation. This estimate is subsequently used to perform a time step of size $\Delta t \gg \delta t$. This combination has been termed *patch dynamics* [25].

In our recent work, we have studied the gap-tooth scheme for a diffusion homogenization problem, which is considered as a model problem. In this case, the microscopic equation is a diffusion equation with a spatially periodic diffusion coefficient with small spatial period ϵ, while the macroscopic (effective) equation describes the averaged behaviour. In the limit of ϵ going to zero, this effective equation is the classical homogenized equation. Our goal is to approximate the effective equation by using only the microscopic equation in a set of small boxes. In [35], we showed that the gap-tooth scheme approximates a finite difference scheme for the homogenized equation, when the averaged gradient is constrained at the box boundaries to reflect the diffusive macroscopic behaviour.

In general, a given microscopic code only allows us to run with a set of predefined boundary conditions. It is highly non-trivial to impose macroscopically inspired boundary conditions on such microscopic codes, see, e.g. [28] for a control-based strategy. We circumvent this problem here by introducing buffer regions at the boundary of each small box, which shield the *short-term* dynamics within the computational domain of interest from boundary effects. One then uses the microscopic code with its *built-in* boundary conditions. This paper is devoted to the study of the resulting *patch dynamics scheme with buffers*, which was already

introduced in [34,35]. We will show that the scheme converges for the diffusion homogenization problem when Dirichlet boundary conditions are used (which clearly do not reflect the correct macroscopic behaviour). We illustrate numerically that the convergence also holds for other boundary conditions, e.g. of no-flux type, and we analyze the relation between buffer size, time step and accuracy. The analysis in this context is important, because we can clearly show the influence of the microscopic scales on the accuracy of the solution for this model problem. However, we emphasize that the real advantage of the method lies in its applicability for non-PDE microscopic simulators, e.g. kinetic Monte-Carlo or molecular dynamics.

We note that many numerical schemes have been devised for the homogenization problem, with the earliest work dating back to Babuska [3] for elliptic problems and Engquist [11] for dynamic problems. Without the aim of being complete, we mention some recent multi-scale approaches to the homogenization problem. The multi-scale finite element method of Hou and Wu [19,20] uses special basis functions to capture the correct microscopic behaviour. Schwab, Matache and Babuska [31,36] have devised a generalized FEM method based on a two-scale finite element space. Other approaches include the use of wavelet projections [8,12] and multi-grid cycles [32]. Runborg et al. [33] proposed a time-stepper based method that obtains the effective behaviour through short bursts of detailed simulations appropriately averaged over many shifted initial conditions. The simulations were performed over the whole domain, but the notion of effective behaviour is identical. In their recent work, E and Engquist and collaborators address the same problem of simulating only the macroscopic behaviour of a multi-scale model, see, e.g. [1,9]. In what they call the heterogeneous multi-scale method, a macro-scale solver is combined with an estimator for quantities that are unknown because the macroscopic equation is not available. This estimator subsequently uses appropriately constrained runs of the microscopic model [9]. It should be clear that the patch dynamics scheme, as introduced in [25], is constructed according to exactly the same principle: by taking a few gap-tooth steps, we estimate the time derivative of the unknown effective equation, and give this as input to an ODE solver, such as projective integration. The difference in their work is that, for conservation laws, the macro-field time derivative is estimated from the flux of the conserved quantity; their generalized Godunov scheme is based on this principle.

This paper is organized as follows. In Section 2, we describe the model homogenization problem. In Section 3, we describe the gap-tooth scheme to approximate the time derivative of the unavailable macroscopic equation. We prove a consistency result and propose a simple heuristic to obtain a sufficient buffer size. We also discuss to what extent the results depend on the specific setting of our model problem. In Section 4, we describe the full patch dynamics algorithm and give some comments on stability. Section 5 contains some numerical examples which illustrate the accuracy and efficiency of the proposed method, and we conclude in Section 6.

2. The homogenization problem

As a model problem, we consider the following parabolic partial differential equation:

$$\begin{aligned} &\partial_t u_\epsilon(x,t) = \partial_x(a(x/\epsilon)\partial_x u_\epsilon(x,t)) \quad \text{in } [0,T)\times[0,1],\\ &u_\epsilon(x,0) = u^0(x) \in L^2([0,1]), \quad u_\epsilon(0,t) = u_\epsilon(1,t) = 0, \end{aligned} \tag{1}$$

where $a(y) = a(x/\epsilon)$ is uniformly elliptic and periodic in y and ϵ is a small parameter. We choose homogeneous Dirichlet boundary conditions for simplicity.

According to classical homogenization theory [6], the solution to (1) can be written as an asymptotic expansion in ϵ,

$$u_\epsilon(x,t) = u_0(x,t) + \sum_{i=1}^{\infty} \epsilon^i (u_i(x,x/\epsilon,t)), \tag{2}$$

where the functions $u_i(x,y,t) \equiv u_i(x,x/\epsilon,t)$, $i = 1, 2, \ldots$ are periodic in y. Here, $u_0(x,t)$ is the solution of the *homogenized equation*

$$\partial_t u_0(x,t) = \partial_x(a^* \partial_x u_0(x,t)) \quad \text{in } [0,T) \times [0,1], \qquad u_0(x,0) = u^0(x) \in L^2([0,1]), \quad u_0(0,t) = u_0(1,t) = 0, \tag{3}$$

the coefficient a^* is the constant effective coefficient, given by

$$a^* = \int_0^1 a(y)\left(1 - \frac{\mathrm{d}}{\mathrm{d}y}\chi(y)\right)\mathrm{d}y \tag{4}$$

and $\chi(y)$ is the periodic solution of

$$\frac{\mathrm{d}}{\mathrm{d}y}\left(a(y)\frac{\mathrm{d}}{\mathrm{d}y}\chi(y)\right) = \frac{\mathrm{d}}{\mathrm{d}y}a(y), \tag{5}$$

the so-called *cell problem*. The solution of (5) is only defined up to an additive constant, so we impose the extra condition

$$\int_0^1 \chi(y)\,\mathrm{d}y = 0.$$

From this cell problem, we can derive $u_1(x,y,t) = \partial_x u_0 \chi(y)$. We note that in one space dimension, an explicit formula is known for a^* [6]

$$a^* = \left[\int_0^1 \frac{1}{a(y)}\,\mathrm{d}y\right]^{-1}. \tag{6}$$

These asymptotic expansions have been rigorously justified in the classical book [6], see also [7]. Under the assumptions made on $a(x/\epsilon)$, one obtains strong convergence of $u_\epsilon(x,t)$ to $u_0(x,t)$ as $\epsilon \to 0$ in $L^2([0,1]) \times C([0,T))$. Indeed, we can write

$$\|u_\epsilon(x,t) - u_0(x,t)\|_{L^2([0,1])} \leqslant C_0 \epsilon \tag{7}$$

uniformly in t.

It is important to note that the gradient of $u(x,t)$ is given by

$$\partial_x u_\epsilon(x,t) = \partial_x u_0(x,t) + \partial_y u_1(x,y,t) + \mathrm{O}(\epsilon), \tag{8}$$

from which it is clear that the micro-scale fluctuations have a strong effect on the local detailed gradient.

Using the gap-tooth scheme, we will approximate the homogenized solution $u_0(x,t)$ by a local spatial average, defined as

$$U(x,t) = \mathscr{S}_h(u_\epsilon)(x,t) = \frac{1}{h}\int_{x-h/2}^{x+h/2} u_\epsilon(\xi,t)\,\mathrm{d}\xi.$$

It can easily be seen that that $U(x,t)$ is a good approximation to $u_0(x,t)$ in the following sense.

Lemma 1. *Consider $u_\epsilon(x,t)$ to be the solution of (1), and $u_0(x,t)$ to be the solution of the associated homogenized equation (3). Then, assuming*

$$h = \mathrm{O}(\epsilon^p), \quad p \in (0,1), \tag{9}$$

the difference between the homogenized solution $u_0(x,t)$ and the averaged solution $U(x,t)$ is bounded by

$$\|U(x,t) - u_0(x,t)\|_{L^\infty([0,1])} \leqslant C_1 h^2 + C_2 \frac{\epsilon}{h}. \tag{10}$$

For a proof, we refer to [35, Lemma 3.1]. Note that this error bound can be improved if we have more knowledge about the convergence of u_ϵ to u_0 (e.g. in $L^\infty([0,1])$).

3. Estimation of the time derivative

We devise a scheme for the evolution of the averaged behaviour $U(x,t)$, while making only use of the given detailed equation (1). Moreover, we assume that a time integration code for (1) has already been written and is available with a number of *standard* boundary conditions, such as no-flux or Dirichlet. We also assume that the order d of the unavailable macroscopic equation (the highest spatial derivative) is known. A strategy to obtain this information is given in [27]. So, we know that the macroscopic equation is of the form

$$\partial_t U = F(U, \partial_x U, \ldots, \partial_x^d U, t), \tag{11}$$

where ∂_t denotes the time derivative and ∂_x^k denotes the kth spatial derivative.

We first describe the gap-tooth scheme with buffers. We discuss the construction of the initial condition and the imposition of *arbitrary* boundary conditions using buffer regions. Subsequently, we show that this scheme converges for the model problem in the limit of growing buffer sizes, when Dirichlet boundary conditions are chosen. We conclude this section with a heuristic for the selection of the buffer size and some general comments.

3.1. The gap-tooth scheme with buffers

Suppose we want to obtain the solution of (11) on the interval [0,1], using an equidistant, macroscopic mesh $\Pi(\Delta x) := \{0 = x_0 < x_1 = x_0 + \Delta x < \cdots < x_N = 1\}$. For convenience, we define a macroscopic comparison scheme, which is a space-time discretization for (11) in the assumption that this equation is known. We will denote the numerical solution of this scheme by $U_i^n \approx U(x_i, t_n)$. Here, we choose as a comparison scheme a forward Euler/spatial finite difference scheme, which is defined by

$$U^{n+\delta} = S(U^n, t_n; \delta t) = U^n + \delta t F(U^n, D^1(U^n), \ldots, D^d(U^n), t_n), \tag{12}$$

where $D^k(U^n)$ denotes a suitable finite difference approximation for the kth spatial derivative.

Since Eq. (11) is not known explicitly, we construct a gap-tooth scheme to approximate the comparison scheme (12). We denote the solution of the gap-tooth scheme by $\bar{U}_i^n \approx U_i^n$. The gap-tooth scheme is now constructed as follows. Consider a small interval (box, *tooth*) of length h around each mesh point, as well as a larger *buffer* interval of size $H > h$ (see Fig. 1). We will perform a time integration using the microscopic model (1) in each box of size H, and we provide this simulation with the following initial and boundary conditions.

3.1.1. Initial condition

We define the initial condition by constructing a local Taylor expansion, based on the (given) box averages $\bar{U}_i^n,\ i = 0, \ldots, N$, at mesh point x_i and time t_n,

$$\bar{u}^i(x, t_n) = \sum_{k=0}^{d} D_i^k(\bar{U}^n) \frac{(x - x_i)^k}{k!}, \quad x \in \left[x_i - \frac{H}{2}, x_i + \frac{H}{2}\right], \tag{13}$$

where d is the order of the macroscopic equation (11). The coefficients $D_i^k(\bar{U}^n),\ k > 0$ are the same finite difference approximations for the kth spatial derivative that would be used in the comparison scheme (12), whereas $D_i^0(\bar{U}^n)$ is chosen such that

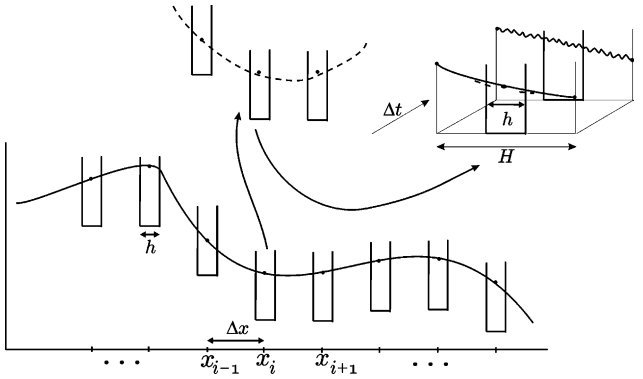

Fig. 1. A schematic representation of the gap-tooth scheme with buffer boxes. We choose a number of boxes of size h around each macroscopic mesh point x_i and define a local Taylor approximation as initial condition in each box. Simulation is performed inside the larger (buffer) boxes of size H, where some boundary conditions are imposed.

$$\frac{1}{h}\int_{x_i-h/2}^{x_i+h/2} \bar{u}^i(\xi,t_n)\,\mathrm{d}\xi = \bar{U}_i^n. \tag{14}$$

For example, when $d=2$, and using standard (second-order) central differences we have

$$D_i^2(\bar{U}^n) = \frac{\bar{U}_{i+1}^n - 2\bar{U}_i^n + \bar{U}_{i-1}^n}{\Delta x^2}, \quad D_i^1(\bar{U}^n) = \frac{\bar{U}_{i+1}^n - \bar{U}_{i-1}^n}{\Delta x}, \quad D_i^0(\bar{U}^n) = \bar{U}_i^n - \frac{h^2}{24}D_i^2(\bar{U}^n). \tag{15}$$

The resulting initial condition was used in [35], where it was derived as an interpolating polynomial for the box averages.

3.1.2. Boundary conditions

The time integration of the microscopic model in each box should provide information on the evolution of the global problem at that location in space. It is therefore crucial that the boundary conditions are chosen such that the solution inside each box evolves *as if it were embedded in the larger domain*. We already mentioned that, in many cases, it is not possible or convenient to impose macroscopically inspired constraints on the microscopic model (e.g. as boundary conditions). However, we can introduce a larger box of size $H > h$ around each macroscopic mesh point, but still only use (for macro-purposes) the evolution over the smaller, inner box. The simulation can subsequently be performed using any of the *built-in* boundary conditions of the microscopic code. Lifting and (short-term) evolution (using *arbitrary* available boundary conditions) are performed in the larger box; yet the restriction is done by processing the solution (here taking its average) over the inner, small box only. The goal of the additional computational domains, the *buffers*, is to buffer the solution inside the small box from the artificial disturbance caused by the (repeatedly updated) boundary conditions. This can be accomplished over *short enough* time intervals, provided the buffers are large enough; analyzing the method is tantamount to making these statements quantitative.

The idea of a buffer region was also introduced in the multi-scale finite element method of Hou (oversampling) [19] to eliminate boundary layer effects; also Hadjiconstantinou makes use of overlap regions to couple a particle method with a continuum code [17]. To avoid confusion, we remark that the introduction of a buffer region in these methods implies that parts of the macroscopic domain are covered more than once, which is an important difference with respect to the method presented here. If the microscopic code allows a choice of different types of microscopic boundary conditions, selecting the size of the buffer may also depend on this choice.

3.1.3. The algorithm

The complete gap-tooth algorithm to proceed from t_n to $t_n + \delta t$ is given below:

(1) **Lifting** At time t_n, construct the initial condition $\bar{u}^i(x, t_n),\ i = 0, \ldots, N$ using the box averages $\bar{U}_i^n$, as defined in (13).
(2) **Simulation** Compute the box solution $\bar{u}^i(x,t),\ t > t_n$, by solving Eq. (1) in the interval $[x_i - H/2, x_i + H/2]$ with *some* boundary conditions up to time $t_{n+\delta} = t_n + \delta t$. The boundary conditions can be anything that the microscopic code allows.
(3) **Restriction** Compute the average $\bar{U}_i^{n+\delta} = 1/h \int_{x_i - h/2}^{x_i + h/2} \bar{u}^i(\xi, t_{n+\delta})\, \mathrm{d}\xi$ over the *inner, small box only*.

It is clear that this procedure amounts to a map of the macroscopic variables $\bar{U}^n$ at time t_n to the macroscopic variables at time $t_{n+\delta}$, i.e., a "coarse to coarse" time δt-map. We write this map as follows:

$$\bar{U}^{n+\delta} = \bar{S}^d(\bar{U}^n, t_n; \delta t, H) = \bar{U}^n + \delta t \bar{F}^d(\bar{U}^n, t_n; \delta t, H), \tag{16}$$

where we introduced the time derivative estimator

$$\bar{F}^d(\bar{U}^n, t_n; \delta t, H) = \frac{\bar{U}^{n+\delta} - \bar{U}^n}{\delta t}. \tag{17}$$

The superscript d denotes the highest spatial derivative that appears in Eq. (11) and has been prescribed by the initialization scheme (13). The accuracy of this estimate depends on the buffer size H, the box size h and the time step δt.

3.2. Consistency

To analyze convergence, we solve the detailed problem approximately in each box. Because $h \gg \epsilon$, we can resort to the homogenized solution, and bound the error using Eq. (7). It is important to note that we use the homogenized equation for analysis purposes only. The algorithm uses box averages of solutions of the detailed problem (1), so it uses only the order d of the homogenized equation, which is required to perform a consistent lifting. We choose to study convergence in the concrete case of Dirichlet boundary conditions, which are guaranteed to introduce boundary artefacts. We will show that these artefacts can be made arbitrarily small by increasing the size of the buffer H. We will show numerically that the results do not depend crucially on the type of boundary conditions.

We first relate the gap-tooth time-stepper as constructed in Section 3.1 to a gap-tooth time-stepper in which the microscopic equation has been replaced by the homogenized equation.

Lemma 2. *Consider the model equation*

$$\partial_t u_\epsilon(x,t) = \partial_x(a(x/\epsilon)\partial_x u_\epsilon(x,t)), \tag{18}$$

where $a(y) = a(x/\epsilon)$ *is periodic in* y *and* $\epsilon \ll 1$, *with initial condition* $u_\epsilon(x,0) = u^0(x)$ *and Dirichlet boundary conditions*

$$u_\epsilon(-H/2,t) = u^0(-H/2), \quad u_\epsilon(H/2,t) = u^0(H/2). \tag{19}$$

For $\epsilon \to 0$, *this problem converges to the homogenized problem*

$$\partial_t u_0(x,t) = \partial_x(a^* \partial_x u_0(x,t)) \tag{20}$$

with initial condition $u_0(x,0) = u^0(x)$ *and Dirichlet boundary conditions*

$$u_0(-H/2,t) = u^0(-H/2), \quad u_0(H/2,t) = u^0(H/2) \tag{21}$$

and the solution of (18) *and* (19) *converges to the solution of* (20) *and* (21), *with the following error estimate*

$$\|u_\epsilon(x,t) - u_0(x,t)\|_{L^2([-H/2,H/2])} \leqslant C_3\epsilon. \tag{22}$$

This is a standard result, whose proof can be found in e.g. [2,7].

We now define two gap-tooth time-steppers. Let

$$\bar{U}^{n+\delta} = \bar{S}^2(\bar{U}^n, t_n; \delta t, H) = \bar{U}^n + \delta t \bar{F}^2(\bar{U}^n, t_n; \delta t, H) \tag{23}$$

be a gap-tooth time-stepper that uses the detailed, homogenization problem (18) and (19) inside each box, and

$$\hat{U}^{n+\delta} = \hat{S}^2(\hat{U}^n, t_n; \delta t, H) = \hat{U}^n + \delta t \hat{F}^2(\hat{U}^n, t_n; \delta t, H) \tag{24}$$

be a gap-tooth time-stepper where the homogenization problem for each box has been replaced by the homogenized equations (20) and (21). The box initialization is done using a quadratic polynomial as defined in (15).

We can apply [35, Lemma 4.2] to bound the difference between $\bar{F}^2(\bar{U}, t_n; \delta t, H)$ and $\hat{F}^2(\hat{U}, t_n; \delta t, H)$.

Lemma 3. *Consider* $\bar{U}^{n+\delta} = \bar{S}^2(\bar{U}^n, t_n; \delta t, H)$ *and* $\hat{U}^{n+\delta} = \hat{S}^2(\hat{U}^n, t_n; \delta t, H)$ *as defined in* (23) *and* (24)*, respectively. Assuming* $\bar{U}^n = \hat{U}^n$, $h = \mathrm{O}(\epsilon^p)$, $p \in (0,1)$, $\epsilon \to 0$, *we have*

$$\|\bar{U}_i^{n+\delta} - \hat{U}_i^{n+\delta}\| \leqslant C_4 \frac{\epsilon}{\sqrt{h}}$$

and therefore

$$\left\|\bar{F}^2(\bar{U}^n, t_n; \delta t, H) - \hat{F}^2(\hat{U}^n, t_n; \delta t, H)\right\| \leqslant C_4 \frac{\epsilon}{\sqrt{h}\delta t}.$$

Again, note that the error estimate can be made sharper if additional knowledge of the convergence of u_ϵ to u_0 is available.

It can easily be checked that the averaged solution $U(x,t)$ also satisfies the diffusion equation (20) for any h in the limit of $\epsilon \to 0$. Therefore, we define the comparison scheme (12) for the model problem as

$$U^{n+\delta} = S(U^n, t_n; \delta t) = U^n + \delta t F(U^n, D^1(U^n), D^2(U^n), t_n) = U^n + \delta t[a^* D^2(U^n)]. \tag{25}$$

We compare the gap-tooth time derivative estimator $\hat{F}^2(\hat{U}, t_n; \delta t, H)$ with the finite difference time derivative used in (25).

Theorem 4. *Consider the gap-tooth time-stepper for the homogenized equation, as defined by* (24)*, and the corresponding comparison scheme* (25)*. Assuming* $U^n = \hat{U}^n$, *and defining the error*

$$E(\delta t, H) = \|\hat{F}^2(\hat{U}^n, t_n; \delta t, H) - a^* D^2(U^n)\|,$$

we have the following result for $\delta t/H^2 \to 0$, $h \ll H$:

$$E(\delta t, H) \leqslant \left(C_1 + C_2 \frac{h^2}{\delta t}\right)\left(1 - \exp\left(-a^* \pi^2 \frac{\delta t}{H^2}\right)\right). \tag{26}$$

Proof. First, we solve Eqs. (20) and (21) analytically inside each box, with initial condition given by (13). Using the technique of separation of variables, we obtain

$$\begin{aligned}\hat{u}^i(x,t) = {} & \hat{U}_i^n - \frac{h^2}{24} D_i^2(\hat{U}^n) + D_i^2(\hat{U}^n)\frac{H^2}{8} + D_i^1(\hat{U}^n)(x - x_i) \\ & + \sum_{m=1}^{\infty} a_m^i \exp\left(-a^* \frac{m^2\pi^2}{H^2}(t - t_n)\right) \sin\left(\frac{m\pi}{H}\left(x - x_i - \frac{H}{2}\right)\right),\end{aligned}$$

where

$$a_m^i = \frac{2}{H}\int_{x_i-H/2}^{x_i+H/2} \frac{1}{2}D_i^2(\hat{U}^n)\left((x-x_i)^2 - \frac{H^2}{4}\right)\sin\left(\frac{m\pi}{H}\left(x - x_i - \frac{H}{2}\right)\right)\mathrm{d}x.$$

This can be simplified to

$$a_m^i = -\frac{2H^2 D_i^2(\hat{U}^n)((-1)^m - 1)}{m^3\pi^3},$$

which yields the following solution:

$$\hat{u}^i(x,t) = \hat{U}_i^n - \frac{h^2}{24}D_i^2(\hat{U}^n) + D_i^2(\hat{U}^n)\frac{H^2}{8} + D_i^1(\hat{U}^n)(x-x_i) + \sum_{m=1}^{\infty}\frac{4H^2 D_i^2(\hat{U}^n)}{(2m-1)^3\pi^3} \times \exp\left(-a^*\frac{(2m-1)^2\pi^2}{H^2}(t-t_n)\right)\sin\left(\frac{(2m-1)\pi}{H}\left(x - x_i - \frac{H}{2}\right)\right). \tag{27}$$

When taking the average over a box of size h, we obtain,

$$\frac{1}{h}\int_{x_i-h/2}^{x_i+h/2}\hat{u}^i(x,t)\,\mathrm{d}x = \hat{U}_i^n - \frac{h^2}{24}D_i^2(\hat{U}^n) + D_i^2(\hat{U}^n)\frac{H^2}{8} + \sum_{m=1}^{\infty}\frac{4H^2\alpha_m}{(2m-1)^3\pi^3}D_i^2(\hat{U}^n) \times \exp\left(-a^*\frac{(2m-1)^2\pi^2}{H^2}(t-t_n)\right), \tag{28}$$

with α_m determined by

$$\begin{aligned}\alpha_m &= \frac{1}{h}\int_{x_i-h/2}^{x_i-h/2}\sin\left(\frac{(2m-1)\pi}{H}\left(x - x_i - \frac{H}{2}\right)\right)\mathrm{d}x \\ &= \frac{H}{(2m-1)h\pi}\left(\cos\left(\frac{(2m-1)\pi}{2H}(H+h)\right) - \cos\left(\frac{(2m-1)\pi}{2H}(H-h)\right)\right) \\ &= (-1)^m\frac{2H}{(2m-1)h\pi}\sin\left(\frac{(2m-1)\pi}{2H}h\right).\end{aligned}$$

The coefficients α_m tend to 1 in absolute value as $h \to 0$. To obtain the time derivative estimate $\hat{F}_i^2(\hat{U}^n, t_n; \delta t, H)$, we proceed as follows:

$$\begin{aligned}\hat{F}_i^2(\hat{U}^n, t_n; \delta t, H) &= \frac{1}{\delta t\, h}\int_{x_i-h/2}^{x_i+h/2}\hat{u}^i(x, t_n+\delta t) - \hat{u}^i(x,t_n)\,\mathrm{d}x \\ &= \frac{1}{\delta t}\sum_{m=1}^{\infty}\frac{4H^2\alpha_m D_i^2(\hat{U}^n)}{(2m-1)^3\pi^3}\left(\exp\left(-a^*\frac{(2m-1)^2\pi^2}{H^2}\delta t\right) - 1\right) \\ &= 4D_i^2(\hat{U}^n)\frac{1}{\xi}\left(\sum_{m=1}^{\infty}\frac{\alpha_m(\exp(-a^*(2m-1)^2\pi^2\xi) - 1)}{(2m-1)^3\pi^3}\right),\end{aligned}$$

where we introduced $\xi = \delta t/H^2$. Using the infinite sum

$$\sum_{m=1}^{\infty}\frac{(-1)^{m+1}}{(2m-1)} = \frac{\pi}{4},$$

it can easily be checked that

$$\lim_{\xi\to 0,h\to 0}\hat{F}_i^2(\hat{U}^n,t_n;\delta t,H)=a^*D_i^2(\hat{U}^n),$$

which already shows that the gap-tooth scheme is consistent in this limit. Obtaining an error bound in terms of ξ is somewhat more involved. We split $\hat{F}_i^2(\hat{U}^n,t_n;\delta t,H)$ as follows,

$$\hat{F}(\hat{U}^n,t_n;\delta t,H)=\hat{F}_1+\hat{F}_2,$$

with and $\hat{F}_1$ and $\hat{F}_2$ defined as:

$$\hat{F}_1=4D_i^2(\hat{U}^n)\frac{1}{\xi}\left(\sum_{m=1}^{\infty}\frac{(-1)^m(\exp(-a^*(2m-1)^2\pi^2\xi)-1)}{(2m-1)^3\pi^3}\right),$$

$$\hat{F}_2=4D_i^2(\hat{U}^n)\frac{1}{\xi}\left(\sum_{m=1}^{\infty}\frac{(\alpha_m-(-1)^m)(\exp(-a^*(2m-1)^2\pi^2\xi)-1)}{(2m-1)^3\pi^3}\right).$$

We have

$$\begin{aligned}\hat{F}_1-a^*D_i^2(\hat{U}^n)&=4D_i^2(\hat{U}^n)\frac{1}{\xi}\left(\sum_{m=1}^{\infty}\frac{(-1)^m(\exp(-a^*(2m-1)^2\pi^2\xi)-1)}{(2m-1)^3\pi^3}\right)-a^*D_i^2(\hat{U}^n)\\&=\frac{4a^*D_i^2(\hat{U}^n)}{\pi}\sum_{m=1}^{\infty}(-1)^{m+1}\left(\frac{1-\exp(-a^*(2m-1)^2\pi^2\xi)}{(2m-1)^3\pi^3\xi}-\frac{\pi}{4}\right).\end{aligned}$$

For notational convenience, we substitute $z=a^*\pi^2\xi$, and we proceed with:

$$\begin{aligned}\left\|\hat{F}_1-a^*D_i^2(\hat{U}^n)\right\|&=\left\|\frac{4D_i^2(\hat{U}^n)a^*}{\pi}\sum_{m=1}^{\infty}(-1)^{m+1}\left(\frac{1-\exp(-(2m-1)^2z)}{(2m-1)^3z}\right)-\frac{\pi}{4}\right\| \qquad (29)\\&\leqslant\left\|\frac{4a^*D_i^2(\hat{U}^n)}{\pi}\left(\frac{\pi}{4}-\sum_{m=1}^{\infty}(-1)^{m+1}\left(\frac{\exp(-(2m-1)^2z)}{2m-1}\right)\right)\right\|\\&\leqslant\left\|\frac{4a^*D_i^2(\hat{U}^n)}{\pi}\left(\sum_{m=1}^{\infty}(-1)^{m+1}\left(\frac{1-\exp(-(2m-1)^2z)}{2m-1}\right)\right)\right\|\\&\leqslant C(1-\exp(-z)). \qquad (30)\end{aligned}$$

It remains to show the asymptotic behaviour of $\hat{F}_2$

$$\begin{aligned}\|\hat{F}_2\|&=\left\|4D_i^2(\hat{U}^n)\sum_{m=1}^{\infty}(-1)^m\frac{\left(\sin\left(\frac{(2m-1)\pi h}{2H}\right)\frac{2H}{(2m-1)\pi h}-1\right)}{(2m-1)^3\pi^3\xi}(\exp(-a^*(2m-1)^2\pi^2\xi)-1)\right\|\\&\leqslant C\left(\frac{\sin(\frac{\pi h}{2H})\frac{2H}{\pi h}-1}{\xi\pi^3}\right)(1-\exp(-a^*\pi^2\xi))\leqslant C\frac{h^2}{H^2}\frac{1-\exp(-a^*\pi^2\xi)}{\xi\pi^3}\\&\leqslant C\frac{h^2}{\delta t}(1-\exp(-a^*\pi^2\xi)). \qquad (31)\end{aligned}$$

The combination of (30) and (31) proves the theorem. □

Remark that the error bound (30) is quite pessimistic, which is illustrated in Fig. 2. Indeed, as $z\to 0$, the error (29) approaches zero much more rapidly than the estimate (30). However, the main behaviour is clear: by choosing the buffer size H large enough with respect to the time-step δt, one can avoid artefacts being

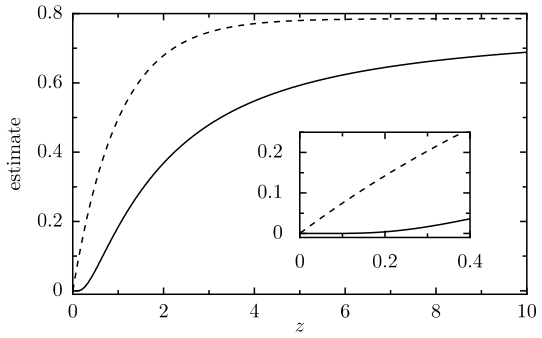

Fig. 2. Error of the gap-tooth estimator according to Eq. (29) (solid) and the estimate (30) (dashed). Inset: zoom around the origin.

caused by the boundary conditions. For this problem, we also see that the error approaches a constant as $z \to \infty$. This is the case where the time-step δt is chosen much too large, such that the problems inside each box have converged to steady-state due to the Dirichlet boundary conditions.

We illustrate this result numerically.

Example 5. Consider the model problem (20) with a $a^* = 0.45825686$ as a microscopic problem on the domain [0,1] with homogeneous Dirichlet boundary conditions and initial condition $u(x,0) = 1 - 4(x - 1/2)^2$. To solve this microscopic problem, we use a second-order finite difference discretization with mesh width $\delta x = 2 \times 10^{-7}$ and `lsode` [18] as time-stepper. The concrete gap-tooth scheme for this example is defined by the initialization (15). We compare a gap-tooth step with $h = 2 \times 10^{-3}$ and $\Delta x = 1 \times 10^{-1}$ with the reference estimator $a^* D^2(\hat{U}^n)$. Fig. 3 shows the error with respect to the finite difference time derivative as a function of H (left) and δt (right). It is clear the convergence is in agreement with Theorem 4. The stagnation for large buffer sizes is due to the finite accuracy of the microscopic solver.

We are now ready to state the general consistency result.

Theorem 6. *Let $\bar{U}^{n+\delta} = \bar{S}^2(\bar{U}^n, t_n; \delta t, H)$ be a gap-tooth time-stepper for the homogenization problem (18) and (19), as defined in (23), and $U^{n+\delta} = S(U^n, t_n; \delta t)$ a comparison finite difference scheme as defined in (25). Then, assuming $U^n = \bar{U}^n$, we have*

$$\|\bar{F}^2(\bar{U}^n, t_n; \delta t, H) - a^* D^2(U^n)\| \leqslant C_4 \underbrace{\frac{\epsilon}{\sqrt{h}\delta t}}_{\text{micro-scales}} + C_5 \underbrace{\left(1 + \frac{h^2}{\delta t}\right)}_{\text{averaging}} \underbrace{\left(1 - \exp(-a^* \pi^2 \frac{\delta t}{H^2})\right)}_{\text{boundary conditions}}. \tag{32}$$

Proof. This simply follows by combining Theorem 4 with Lemma 2. □

Formula (32) shows the main consistency properties of the gap-tooth estimator. The error decays exponentially as a function of buffer size, but the optimal accuracy of the estimator is limited by the presence of the microscopic scales. Therefore, we need to make a trade-off to determine an optimal choice for H and δt. The smaller δt, the smaller H can be used to reach optimal accuracy (and thus the smaller the computational cost), but smaller δt implies a larger optimal error. This is illustrated in the following numerical example.

Example 7. Consider the model problem (18) with

$$a(x/\epsilon) = 1.1 + \sin(2\pi x/\epsilon), \quad \epsilon = 1 \times 10^{-5} \tag{33}$$

as a microscopic problem on the domain [0,1] with homogeneous Dirichlet boundary conditions and initial condition $u(x,0) = 1 - 4(x - 1/2)^2$. This diffusion coefficient has also been used as a model example in

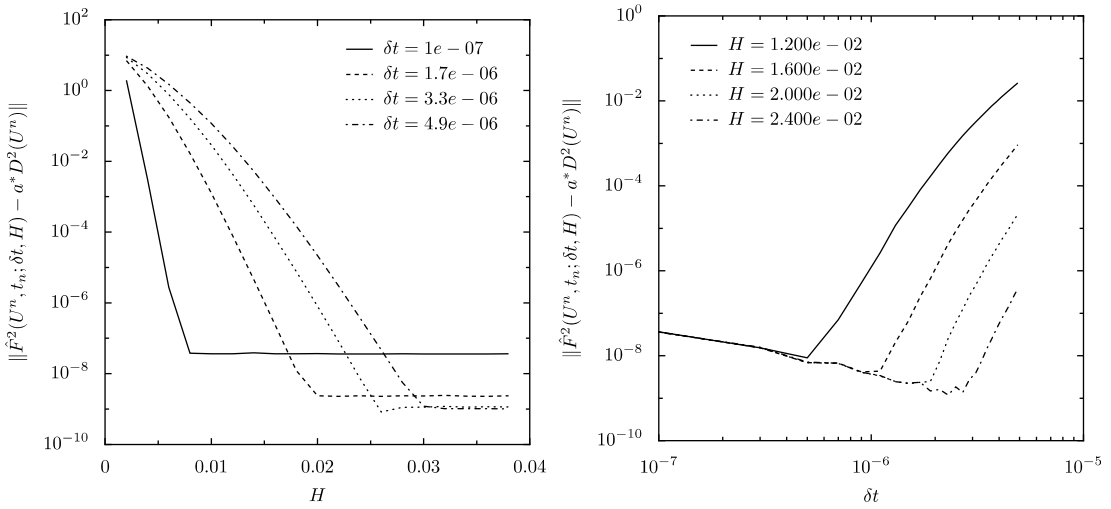

Fig. 3. Error of the gap-tooth estimator $\hat{F}^2(U^n, t_n; \delta t, H)$ (which uses the homogenized problem (20) and (21) inside each box) with respect to the finite difference time derivative $a^* D^2(U^n)$ on the same mesh. (Left) Error with respect to H for fixed δt. (Right) Error with respect to δt for fixed H.

[1,35]. To solve this microscopic problem, we use a second-order finite difference discretization with mesh width $\delta x = 1 \times 10^{-7}$ and `lsode` as time-stepper. The concrete gap-tooth scheme for this example is defined by the initialization (15). We compare a gap-tooth step with $h = 2 \times 10^{-3}$ and $\Delta x = 1 \times 10^{-1}$ with the reference estimator $a^* D^2(\bar{U}^n)$, in which the effective diffusion coefficient is known to be $a^* = 0.45825686$. Fig. 4 shows the error with respect to the finite difference time derivative as a function of H (left) and δt (right). It is clear that the convergence is in agreement with Theorem 6. We see that smaller values of δt result in larger values for the optimal error, but the convergence towards this optimal error is faster.

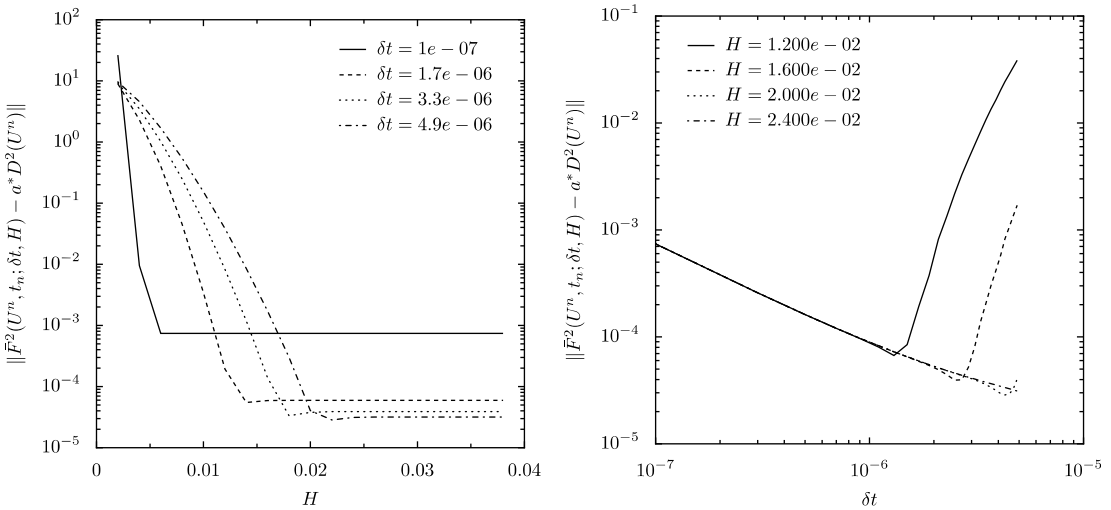

Fig. 4. Error of the gap-tooth estimator $\bar{F}(U^n, t_n; \delta t, H)$ (which uses the detailed, homogenization problem (18) and (19) inside each box) with respect to the finite difference time derivative $a^* D^2(U^n)$ on the same mesh. (Left) Error with respect to H for fixed δt. (Right) Error with respect to δt with fixed H.

3.3. Choosing the method parameters

When performing time integration using patch dynamics, one must determine a macroscopic mesh width Δx, an inner box size h, a buffer box size H and a time step δt. These method parameters need to be chosen adequately to ensure an accurate result. Since the gap-tooth estimator approximates the time derivative that would be obtained through a method-of-lines discretization of the macroscopic equation, the macroscopic mesh width Δx can be determined by macroscopic properties of the solution only, enabling reuse of existing remeshing techniques for PDEs. The box width h has to be sufficiently large to capture all small scale effects, but small enough to ensure a good spatial resolution. Here, we just choose $h \gg \epsilon$. In our simplified setting, where the microscopic model is also a partial differential equation, we are free to choose δt, which allows us to illustrate the convergence properties of the method. However, in practical problems, the choice of δt will be problem-dependent, since it will need to be chosen large enough to deduce reliable information on the macroscopic time derivative.

Therefore, we focus on determining the buffer width H, assuming that all other parameters have already been fixed. From Theorem 6, it follows that the desired value of H depends on the effective diffusion coefficient a^*, which is unknown. We thus need to resort to a heuristic. Consider the model problem (18) and (19) inside one box, centered around $x_0 = 5 \times 10^{-1}$, with $H = 8 \times 10^{-3}$, and initial condition $u^0(x) = 1 - 4(x - 1/2)^2$. The diffusion coefficient is given by (42), see Example 7. Denote the solution of this problem by $\bar{u}(x,t)$, and define

$$\bar{F}(x,t) = \frac{1}{t}\mathcal{S}_h(\bar{u}(x,t) - \bar{u}(x,0)) = \frac{1}{t}\int_{x-h/2}^{x+h/2} \frac{\bar{u}(\xi,t) - \bar{u}(\xi,0)}{h}\,\mathrm{d}\xi \tag{34}$$

with $h = 2 \times 10^{-3}$ and $x \in [(-H+h)/2,(H-h)/2]$. Fig. 5(left) shows $\bar{F}(x,t)$ for a number of values of t. We clearly see how the error in the estimator propagates inwards from the boundaries. The same function is plotted on the right, only now the microscopic model is the reaction–diffusion equation

$$\begin{aligned} &\partial_t u_\epsilon(x,t) = \partial_x(a(x/\epsilon)\partial_x u_\epsilon(x,t)) + u_\epsilon(x,t)\left(1 - \frac{u_\epsilon(x,t)}{1.2 + \sin(2\pi x)}\right), \\ &u_\epsilon(-H/2,t) = u^0(-H/2), \quad u_\epsilon(H/2,t) = u^0(H/2), \end{aligned} \tag{35}$$

again with $a(x/\epsilon)$ defined as in (42). In the presence of reaction terms, $\bar{F}(x,t)$ is no longer constant in the internal region. Based on these observations, we propose the following test for the quality of the buffer size,

$$\|\bar{F}(0,\delta t) - \bar{F}(0,(1-\alpha)\delta t)\| < \mathtt{Tr}, \quad 0 < \alpha \ll 1. \tag{36}$$

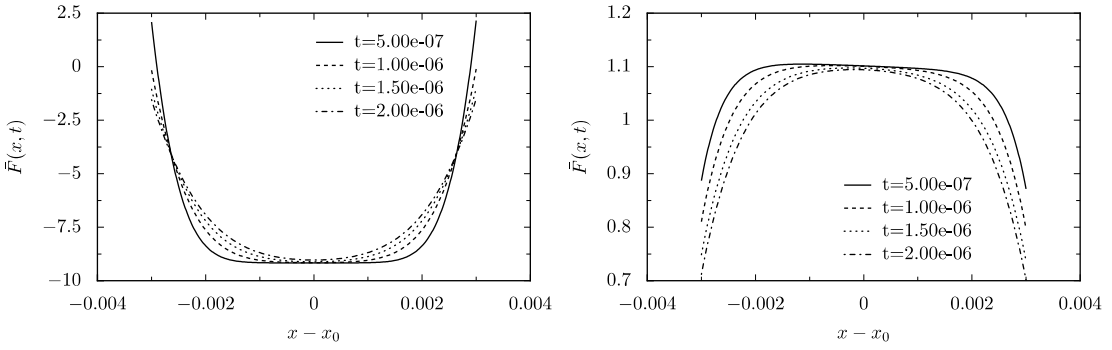

Fig. 5. The function $\bar{F}(x,t)$ as defined in Eq. (34) for a number of values of time, using a buffer size $H = 8 \times 10^{-3}$ and $h = 2 \times 10^{-3}$. (Left) the model diffusion problem (18) and (19). (Right) The reaction–diffusion equation (35). The estimate clearly gets affected by the boundary conditions as time advances.

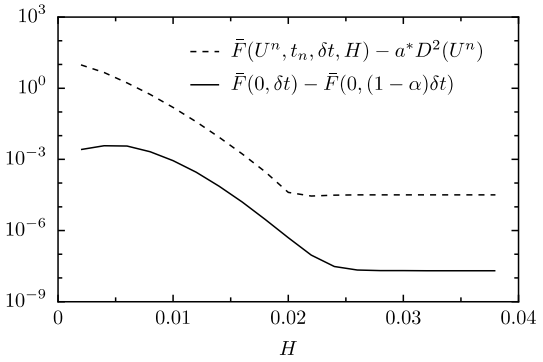

Fig. 6. Error of the gap-tooth estimator (dashed) and heuristic error estimate (solid) as a function of buffer size for the model equation (18) with diffusion coefficient (42) for $\delta t = 5 \times 10^{-6}$ and $\alpha = 0.04$.

Fig. 6 shows this heuristic, together with the error, as a function of H for $\delta t = 5 \times 10^{-6}$ and $\alpha = 0.04$. It is clear that the computed quantity in (36) is proportional to the error for sufficiently large H. However, this heuristic is far from perfect, since the simulations inside each box can converge to a steady-state due to the Dirichlet boundary conditions. If this steady-state is reached in a time interval smaller than δt, Eq. (36) will underestimate the error, resulting in an insufficient buffer size H getting accepted. However, as soon as the problem-dependent parameters α and `Tr` have been determined, this heuristic can be used during the simulation to check whether the currently used buffer size is still sufficient.

3.4. Discussion

3.4.1. Other boundary conditions

In Section 3.2, we studied the convergence of the gap-tooth estimator both analytically and numerically in the case of Dirichlet boundary conditions. We will now show numerically that the results obtained in that section do not depend crucially on the type of boundary conditions. Consider again the diffusion problem (18), with the diffusion coefficient defined as in (42), see also Example 7. We construct the gap-tooth time derivative estimator $\bar{F}(U^n, t_n; \delta t, H)$ as outlined in Section 3.1, but now we use no-flux instead of Dirichlet boundary conditions. In each box, we then solve the following problem:

$$\partial_t u_\epsilon(x,t) = \partial_x(a(x/\epsilon)\partial_x u_\epsilon(x,t)), \qquad \partial_x u_\epsilon(-H/2,t) = 0, \quad \partial_x u_\epsilon(H/2,t) = 0. \tag{37}$$

The concrete gap-tooth scheme that is used, as well as the corresponding finite difference comparison scheme, are defined by the initialization (15). Fig. 7 shows the error with respect to the finite difference time derivative $a^* D^2(U^n)$. We see qualitatively the same behaviour as for Dirichlet boundary conditions.

In general, the choice of boundary conditions might influence the required buffer size. In the ideal case, where the boundary conditions are chosen to correctly mimic the behaviour in the full domain, we can choose $H = h$. Then there is no buffer and the computational complexity is, in some sense, optimal. For reaction–diffusion homogenization problems, this can be achieved by constraining the averaged gradient around each box edge [35]. In situations where the correct boundary conditions are not known, or prove impossible to implement, one is forced to resort to the use of buffers.

3.4.2. Microscopic simulators

It is possible that the microscopic model is not a partial differential equation, but some microscopic simulator, e.g. kinetic Monte-Carlo or molecular dynamics code. In fact, this is the case where we expect our method to be most useful. In this case, the *lifting* step, i.e., the construction of box initial conditions,

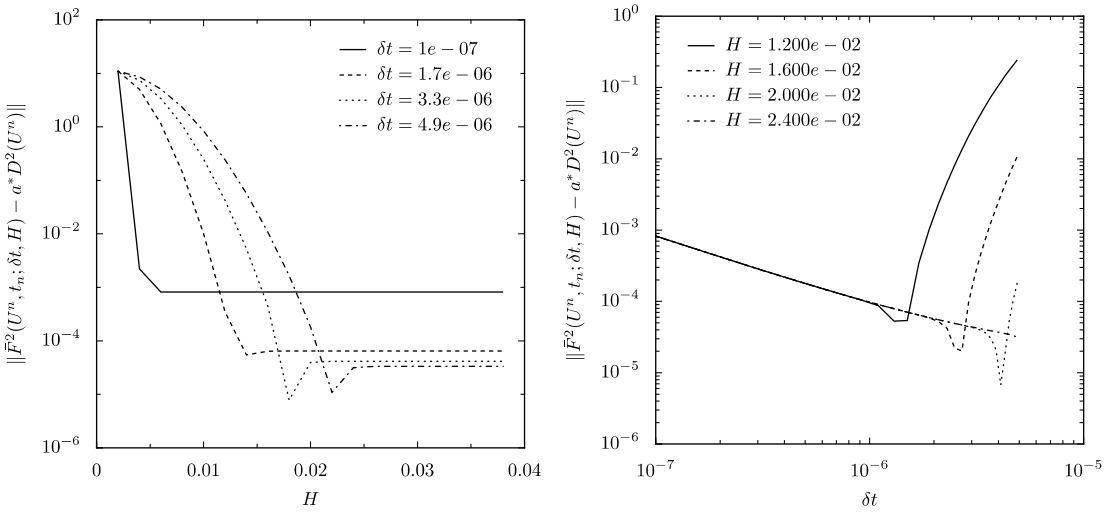

Fig. 7. Error of the gap-tooth estimator $\bar{F}(U^n,t_n;\delta t,H)$ (using the microscopic problem (37) with diffusion coefficient (42) in each box) with respect to the finite difference time derivative $a^*D^2(U^n)$ on the same mesh.

becomes more involved. In general, the microscopic model will have many more degrees of freedom, the *higher order moments* of the evolving distribution. These will quickly become slaved to the governing moments (the ones where the lifting is conditioned upon), see, e.g. [25,29]. The crucial assumption in Theorem 6 is that the solution in each box evolves according to the macroscopic equation. For a microscopic simulation, this will usually mean that we need to construct an initial condition in which, for example, a number of higher order moments are already slaved to the governing moments (so-called *mature* initial conditions). To this end, it is possible to perform a constrained simulation before initialization to create such mature initial conditions [14,21]. If this is not done, the resulting evolution may be far from what is expected, see [43] for an illustration in the case of a lattice-Boltzmann model.

4. Patch dynamics

Once a good gap-tooth time derivative estimator has been constructed, it can be used as a method-of-lines spatial discretization in conjunction with any time integration scheme. Consider for concreteness the forward Euler scheme for (11) (the comparison scheme), given by

$$U^{n+1} = U^n + \Delta t F(U^n, D^1(U^n), \ldots, D^d(U^n), t_n), \tag{38}$$

which we will abbreviate as

$$U^{n+1} = U^n + \Delta t F(U^n, t_n) \tag{39}$$

and the corresponding patch dynamics scheme

$$\bar{U}^{n+1} = \bar{U}^n + \Delta t \bar{F}^d(\bar{U}^n, t_n; \delta t, H), \tag{40}$$

where $\bar{F}^d(\bar{U}^n,t_n;\delta t,H)$ is defined as in (17). Theorem 6 establishes the consistency of the gap-tooth estimator. In order to obtain convergence, we also need to show stability. In [9], E and Engquist state that the heterogeneous multi-scale method is stable if the corresponding comparison scheme is stable, see [9, Theorem 5.5]. This theorem would also apply to our case. However, due to the assumption that the numerical

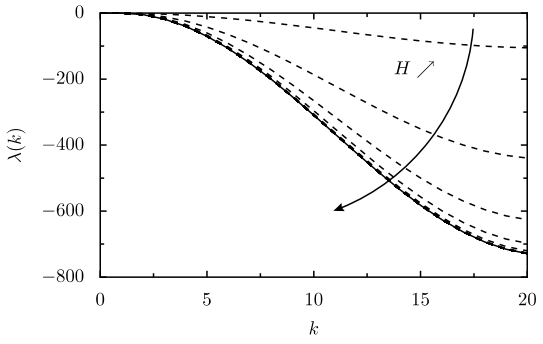

Fig. 8. Spectrum of the estimator $\bar{F}(U^n, t_n; \delta t, H)$ (dashed) for the model equation (18) with diffusion coefficient (42) for $H = 2\times10^{-3}$, $4\times10^{-3},\ldots,2\times10^{-2}$ and $\delta t = 5\times10^{-6}$, and the eigenvalues (41) of $F(U^n,t_n)$ (solid).

approximation satisfies certain boundedness criteria, it may be of little practical value. In our work, we circumvent some of these difficulties by studying the stability properties of the scheme *numerically*. This can be done by computing the eigenvalues of the time derivative estimator as a function of H.

Consider the homogenization diffusion equation (18) with the diffusion coefficient $a(x/\epsilon)$ given by (42). The homogenized equation is given by (20) with $a^* = 0.45825686$. In this case, the time derivative operator $F(U^n,t_n)$ in the comparison scheme (38) has eigenvalues

$$\lambda_k = -\frac{4a^*}{\Delta x^2}\sin^2(\pi k \Delta x), \tag{41}$$

which, using the forward Euler scheme as time-stepper, results in the stability condition

$$\max_k |1 + \lambda_k \Delta t| \leqslant 1 \quad \text{or} \quad \frac{\Delta t}{\Delta x^2} \leqslant \frac{1}{2}a^*.$$

It can easily be checked that the operator $\bar{F}(U^n, t_n; \delta t, H)$ is linear, so we can interpret the evaluation of $\bar{F}(U^n, t_n; \delta t, H)$, as a matrix–vector product. We can therefore use any matrix-free linear algebra technique to compute the eigenvalues of $\bar{F}(U^n, t_n; \delta t, H)$, e.g. Arnoldi. We choose to compute $\bar{F}(U^n, t_n; \delta t, H)$ and $F(U^n,t_n)$ on the domain [0,1] with Dirichlet boundary conditions, on a mesh of width $\Delta x = 0.05$ and with an inner box width of $h = 2\times10^{-3}$. We choose $\delta t = 5\times10^{-6}$ and compute the eigenvalues of $\bar{F}(U^n, t_n; \delta t, H)$ as a function of H. The results are shown in Fig. 8. Two conclusions are apparent: since the most negative eigenvalue for $\bar{F}(U^n, t_n; \delta t, H)$ is always smaller in absolute value than the corresponding eigenvalue of $F(U^n,t_n)$ the patch dynamics scheme is always stable if the comparison scheme is stable. Moreover, we see that, with increasing buffer size H, the eigenvalues of $\bar{F}(U^n, t_n; \delta t, H)$ approximate those of $F(U^n,t_n)$, which is an indication of consistency.

5. Numerical results

We will consider three example systems to illustrate the method. First, we will briefly illustrate the method on a pure diffusion problem. The second example is a system of two coupled reaction–diffusion equations, which models CO oxidation on a heterogeneous catalytic surface. Due to the reaction term, the proof of Theorem 6 is strictly speaking not valid, but nevertheless the conclusions are the same. The third example is the Kuramoto–Sivashinsky equation. This fourth-order non-linear parabolic equation is widely used, e.g. in combustion modeling. The patch dynamics scheme with buffers also works in this case, showing that the method can also be applied when the macroscopic equation is of higher order. All computations were performed in Python, making use of the SciPy package [22] for scientific computing.

5.1. Example 1: Diffusion problem

We consider the model problem (18) with

$$a(x/\epsilon) = 1.1 + \sin(2\pi x/\epsilon), \quad \epsilon = 1 \times 10^{-5} \tag{42}$$

as a microscopic problem on the domain [0,1] with homogeneous Dirichlet boundary conditions and initial condition $u(x,0) = 1 - 4(x - 1/2)^2$. This diffusion coefficient has also been used as a model example in [1,35]. To solve this microscopic problem, we use a second-order finite difference discretization with mesh width $\delta x = 1 \times 10^{-7}$ and `lsode` as time-stepper. The concrete gap-tooth scheme for this example is defined by the initialization (15).

In Section 3, we have already shown the consistency of the gap-tooth estimator. The properties for the macroscopic scheme are chosen to be $\Delta x = 1 \times 10^{-1}$ and $\Delta t = 1 \times 10^{-3}$. As gap-tooth parameters, we choose $H = 8 \times 10^{-3}$, $\delta t = 1 \times 10^{-6}$ and $h = 1 \times 10^{-4}$. Thus, simulations are performed in only 8% of the spatial domain, and 0.1% of the time domain.

We perform a gap-tooth simulation using these parameters up to time $t = 0.5$, which we compare with a simulation of the effective equation using the finite difference comparison scheme on the same grid. The results are shown in Fig. 9. We also compare the results of the patch dynamics scheme to a reference solution of the effective equation, which is obtained using the comparison scheme on a much finer grid ($\Delta x = 5 \times 10^{-3}$ and $\Delta t = 1 \times 10^{-6}$). We see that the solution is well approximated, and that the error of the patch dynamics scheme with respect to the finite difference comparison scheme is an order of magnitude smaller than the total error with respect to the reference solution.

5.2. Example 2: A non-linear travelling wave in a heterogeneous excitable medium

Consider the following system of two coupled reaction–diffusion equations,

$$\begin{aligned} \partial_t u(x,t) &= \partial_x^2 u(x,t) + \frac{1}{\delta} u(x,t)(1 - u(x,t))\left(u(x,t) - \frac{w(x,t) + b(x)}{a(x)}\right), \\ \partial_t w(x,t) &= g(u(x,t)) - w(x,t), \end{aligned} \tag{43}$$

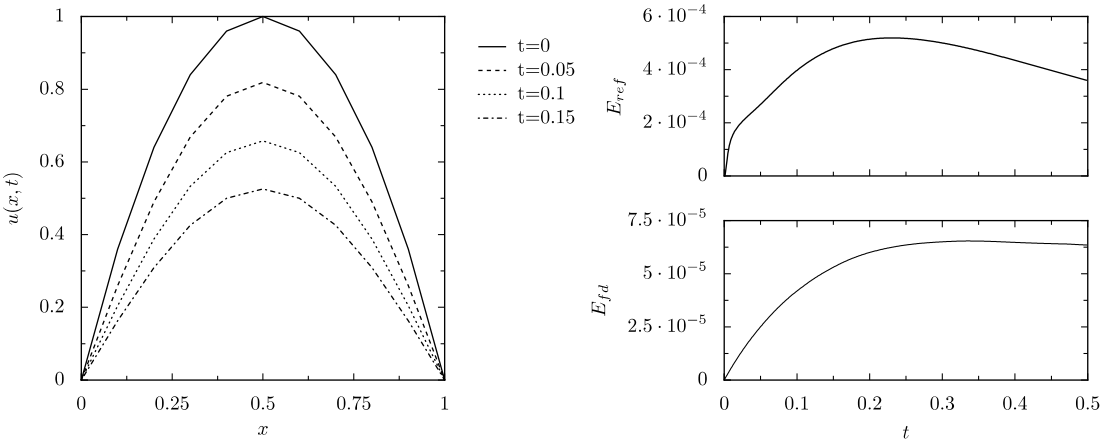

Fig. 9. (Left) Snapshots of the solution of the homogenization diffusion equation using the patch dynamics scheme at certain moments in time. (Right) Error with respect to the "exact" solution of the effective equation (top) and a finite difference comparison scheme (bottom). The total error is dominated by the error of the finite difference scheme.

with

$$g(u) = \begin{cases} 0, & u < 1/3, \\ 1 - 6.75u(1-u)^2, & 1/3 \leqslant u < 1, \\ 1, & u \geqslant 1. \end{cases} \tag{44}$$

This equation models the spatiotemporal dynamics of CO oxidation on microstructured catalysts, which consist of, say, alternating stripes of two different catalysts, such as platinum, Pt, and palladium, Pd, or platinum and rhodium, Rh [16,5,40]. The goal is to improve the average reactivity or selectivity by combining the catalytic activities of the different metals, which are coupled through surface diffusion. In the above model, u corresponds to the surface concentration of CO, w is a so-called surface reconstruction variable and $g(u)$ is an experimentally fitted sigmoidal function. Details can be found in [23,4].

In this model a and b and the time-scale ratio parameter δ are physical parameters that incorporate the experimental conditions: partial pressures of O_2 and CO in the gas phase, temperature, as well as kinetic constants for the surface. Here, we will study a domain of length $L = 21$ with a periodically varying medium: a striped surface that can be thought of as consisting of equal amounts of Pt and Rh, with stripe width $\epsilon/2$. The medium is then defined by

$$a(x) = 0.84, \quad b(x) = -0.025 + 0.725\sin(2\pi x/\epsilon), \quad \delta = 0.025. \tag{45}$$

This particular choice of parameters is taken from [33], where an effective bifurcation analysis for this model was presented. For these parameter values, the effective equation, given by (43) and (44) with

$$a(x) = 0.84, \quad b(x) = -0.025, \quad \delta = 0.025, \tag{46}$$

supports travelling waves. It was shown in [33] that this conclusion remains true for the given heterogeneity. This was done by computing the effective behaviour as the average of a large number of spatially shifted realization of the wave. Here, using the gap-tooth scheme, the solution is spatially averaged inside each box, but the notion of effective behaviour is identical. We choose the small scale parameter $\epsilon = 1 \times 10^{-4}$.

The macroscopic comparison scheme for the effective equations (43)–(46) is defined as a standard second-order central difference discretization in space on a macroscopic mesh of width $\Delta x = 0.25$, combined with a forward Euler time-stepper. The time-step is chosen as $\Delta t = 1 \times 10^{-2}$, which ensures stability. The patch dynamics scheme for the detailed equations (43)–(45) is then obtained by using a gap-tooth estimator for the time derivative using the initialization (15) with the same forward Euler time-stepper.

5.2.1. Accuracy

We perform a numerical simulation for this model on the domain $[0,L]$ using the patch dynamics scheme. The gap-tooth parameters are given by $h = 5 \times 10^{-4}$, $H = 1.5 \times 10^{-2}$ and $\delta t = 5 \times 10^{-7}$. Inside each box, we used a finite difference approximation in space, with mesh width $\delta x = 1 \times 10^{-6}$ and `lsode` as time-stepper. The initial condition is given by

$$u(x,0) = \begin{cases} 1, & x \in [8,18], \\ 0, & \text{else}, \end{cases} \qquad w(x,0) = \begin{cases} 0.5 - 0.05x, & x \leqslant 8, \\ 0.07x - 0.46, & 8 < x \leqslant 18, \\ -0.1x + 2.6, & x > 18. \end{cases}$$

The results are shown in Fig. 10. We clearly see both the initial transient and the final travelling wave solution. For comparison purposes, the same computation was performed using the finite difference comparison scheme for the effective equation. We also computed an "exact" solution for the effective equation using a much finer grid ($\Delta x = 5 \times 10^{-3}$ and $\Delta t = 1 \times 10^{-5}$). Fig. 11 shows the errors of the patch dynamics simulation with respect to the finite difference simulation of the effective equation and the "exact" solution, respectively. We clearly see that the patch dynamics scheme is a very good approximation of the finite difference scheme, and the error with respect to the exact solution is dominated by the error of the finite difference scheme.

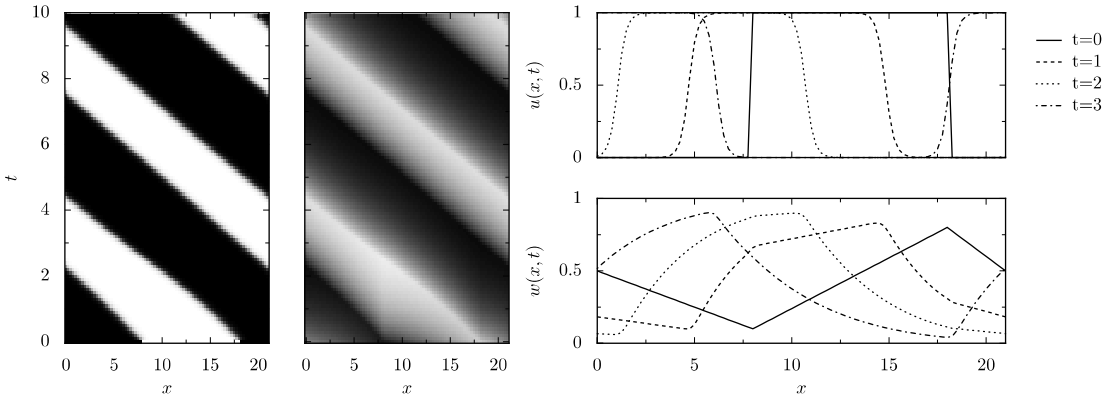

Fig. 10. (Left) Solution of Eqs. (43)–(45) using the patch dynamics scheme as a function of space and time. Colors indicate values (black = 1, white = 0). (Right) Snapshots of the solution at certain moments in time, clearly showing the approach to a travelling wave solution.

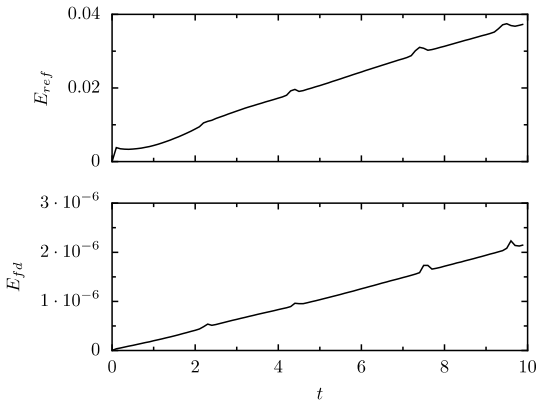

Fig. 11. Error of a patch dynamics simulation for Eqs. (43)–(45) with respect to the "exact" solution of the effective equation (top) and a finite difference comparison scheme (bottom). The error is dominated by the error of the finite difference scheme.

5.2.2. *Efficiency*

Time integration using the patch dynamics scheme is more efficient than a complete simulation using the microscopic model, since the microscopic model is used only in small portions of the space-time domain (the patches). An obvious (but not always correct) way to study the efficiency is to compare the size of the total space-time domain with the size of the patches. In this example, the simulations are only performed in 6% of the spatial domain. Of course, when it is possible to apply physically correct boundary conditions around the inner box, the buffer boxes are not necessary, and the boxes would only cover 0.2% of the space domain. For reaction–diffusion homogenization problems, we showed that buffer boxes are not required when we constrain the average gradient at the box boundary [35]. The gain in the spatial dimension is determined by the separation in spatial scales. It can be large when the macroscopic solution is smooth (few macroscopic mesh points are needed) and propagation of boundary artefacts is slow (small buffer box is sufficient). Note that in higher spatial dimensions, this gain can be even more spectacular.

The gain in the temporal dimension can be determined similarly. In the example of Section 5.2, the gap-tooth step was chosen as $\delta t = 5 \times 10^{-7}$, whereas for macroscopic time integration, the forward Euler

scheme was used with $\Delta t = 1 \times 10^{-2}$. Therefore, in the temporal dimension, we gain a factor of 2×10^5. In more realistic applications, when the microscopic model is not a partial differential equation, we expect this gain to be smaller, since additional computational effort will be required to remove the errors that were introduced during the lifting step, e.g. in the form of constrained simulation [14].

5.3. Example 3: Kuramoto–Sivashinsky equation

In the third example, we will show that the patch dynamics scheme is able to recover fourth-order macroscopic behaviour. To this end, we consider the Kuramoto–Sivashinsky equation

$$\partial_t u(x,t) = -v\partial_x^4 u(x,t) - \partial_x^2 u(x,t) - u(x,t)\partial_x u(x,t), \quad x \in [0, 2\pi] \tag{47}$$

with periodic boundary conditions. This equation is frequently used in the modelling of combustion and thin film flow. For the parameter value $v = 4/15$, it has been shown that the equation supports travelling wave solutions, see, e.g. [26]. In our computations, the "microscopic" behaviour that will be simulated inside the patches is governed by the Kuramoto–Sivashinsky equation, while the finite difference comparison scheme, that we wish to approximate, is a discretization of the same Kuramoto–Sivashinsky equation on the coarse grid. Therefore, we are not interested in the coarse-grained, statistical behaviour of this equation, as it was studied in e.g. [10]. Instead, we consider this example as an "analysis problem", since the microscopic and macroscopic dynamics both satisfy the same Eq. (47), and study whether the patch dynamics scheme is also consistent when the macroscopic equation is of fourth order.

We note that the approach taken here is not advocated as a good way to solve the Kuramoto–Sivashinsky equation. Indeed, due to a lack of scale separation in this model, we do not expect to be able to use very small patches, and this statement will be quantified below. Nevertheless, we can show that the patch dynamics time-stepper converges to a finite difference approximation for this equation on the coarse grid.

To obtain the macroscopic comparison scheme, we discretize the second and fourth-order spatial derivatives using second-order central differences, on a macroscopic mesh of width $\Delta x = 0.05\pi$, combined with a forward Euler time integrator with time-step $\Delta t = 1 \times 10^{-5}$. This small macroscopic time-step arises due to the stiffness of the effective equation. We can accelerate timestepping by wrapping a so-called *projective integration method* around the forward Euler scheme [13]. This scheme works as follows. First, we perform a number of forward Euler steps,

$$U^{k+1,N} = U^{k,N} + \Delta t F(U^{k,N}, t_n),$$

where, for consistency, $U^{0,N} = U^N$, followed by a large extrapolation step

$$U^{N+1} = (M+1)U^{k+1,N} - MU^{k,N}, \quad M > k.$$

Here, $U^{k,N} \approx U(N(M+k+1)\Delta t + k\Delta t)$. The parameters k and M determine the stability region of the resulting time-stepper. An analysis of these methods is given in [13]. It can be checked that, for this equation, choosing $k = 2$ and $M = 7$ results in a stable time-stepping scheme.

The patch dynamics scheme is constructed by replacing the time derivative $F(U^{k,N}, t_n)$ by a gap-tooth estimator $\bar{F}^4(\bar{U}^{k,N}, t_n; \delta t, H)$, obtained by the initialization (13), where we choose the order of the Taylor expansion to be $d = 4$. The coefficient D_k^i, $k > 0$ are determined by the macroscopic comparison scheme. Inside each box, Eq. (47) is solved, on a mesh of width $\delta x = 1 \times 10^{-5}$, subject to Dirichlet and no-flux boundary conditions, using `lsode` as time-stepper. We fixed the box width $h = 1 \times 10^{-3}$.

5.3.1. Consistency and efficiency

Because of the fourth-order term and the non-linearity, Theorem 6 is not proven. Therefore, we numerically check the consistency of the estimator, by computing the gap-tooth estimator $\bar{F}^4(\bar{U}^{k,N}, t_n; \delta t, H)$ as a function of H for a range of values for δt, and comparing the resulting estimate with the time derivative of

the comparison scheme. As an initial condition, we choose $u^0(x) = \sin(2\pi x)$. The results are shown in Fig. 12(left). We see qualitatively the same behaviour as in Section 3.2 for diffusion problems. There are two main differences. First, in this case the convergence is no longer monotonic, which explains the sharp peaks in the error curves. Also, the scale separation in the Kuramoto–Sivashinsky equation is much smaller than for the diffusion equation. Since boundary artefacts travel inwards much faster, we need to choose the buffer size H fairly large. Therefore, the gain will be much smaller in space. Indeed, the figure suggests that a good compromise between accuracy and efficiency would be to choose $\delta t = 4 \times 10^{-9}$ and $H = 3\pi \times 10^{-2}$. Choosing a larger δt could require H to be so large that the regions start to overlap.

For this choice of the parameters, the computations have to be performed in 60% of the spatial domain. However, for a forward Euler step, we only need to simulate in 1/25,000 of the time-domain. Using the projective integration scheme therefore gives us a total gain factor of about 80,000 in time. Again, we note that in real applications, this spectacular gain will partly be compensated by the additional computational effort that is required to create appropriate initial conditions.

We can draw two main conclusions. The scheme allows to simulate higher order macroscopic equations, and the gain in the space domain is heavily dependent on the separation of scales in the macroscopic equation.

5.3.2. Accuracy

We perform a numerical simulation for this model on the domain [0,2π] using the patch dynamics scheme. The gap-tooth parameters are given by $h = 1 \times 10^{-3}$, $H = 3\pi \times 10^{-2}$ and $\delta t = 4 \times 10^{-9}$. Inside each box, we used a finite difference approximation in space, with mesh width $\delta x = 1 \times 10^{-5}$ and `lsode` as time-stepper. The initial condition is given by

$$u(x,0) = \begin{cases} -1, & x \in [0, 0.8\pi], \\ -1 + 5(x - 0.8\pi), & x \in [0.8\pi, 1.5\pi], \\ 2.5 - 7(x - 1.5\pi), & x \in [1.5\pi, 2\pi]. \end{cases}$$

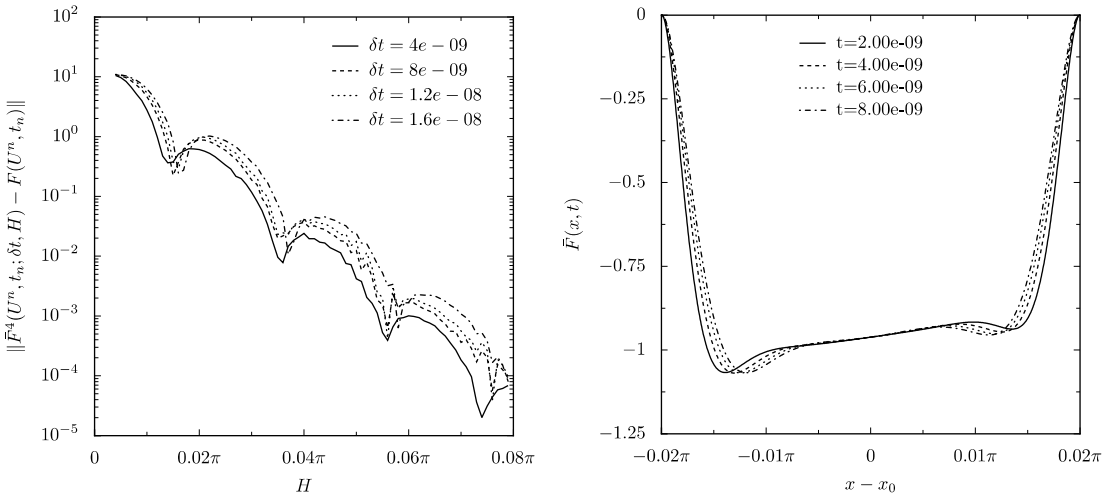

Fig. 12. (Left) Error of the gap-tooth estimator $\bar{F}(\bar{U}^{0,0}, t_n; \delta t, H)$ with respect to the finite difference time derivative $F(U^{0,0}, t_n)$. (Right) The function (34) as a function of x for a number of values of time. We clearly see how the estimate gets affected by the boundary conditions.

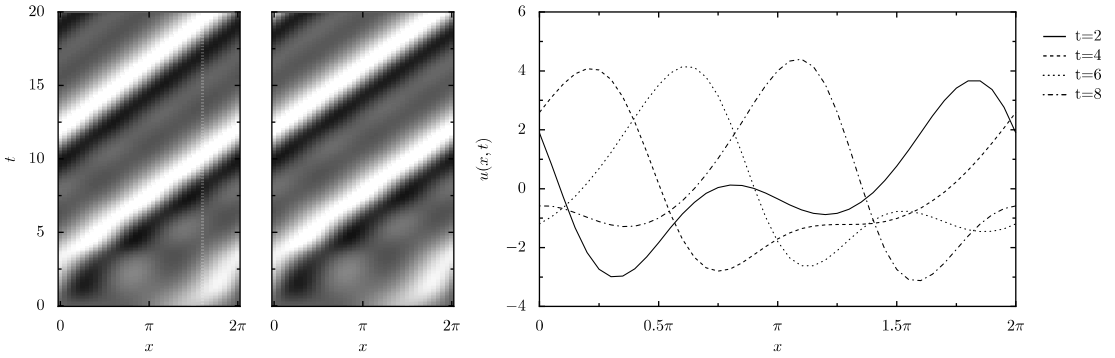

Fig. 13. (Left) Solution of Eq. (47) using the patch dynamics scheme as a function of space and time. Colors indicate values (black = 4, white = −4). (Right) Snapshots of the solution at certain moments in time, clearly showing the approach to a travelling wave solution.

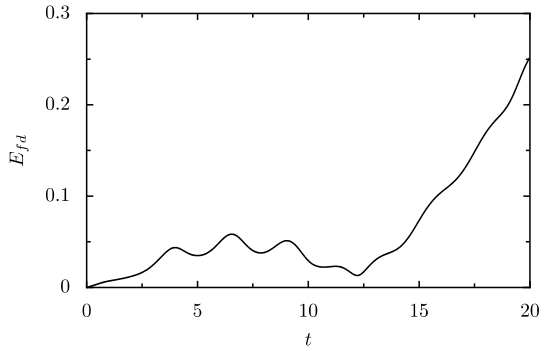

Fig. 14. Error of a patch dynamics simulation for Eq. (47) with respect to the a finite difference comparison scheme for the effective equation. We see that this error grows monotonic once the travelling wave has been reached, due to a slight difference in propagation speed.

The results are shown in Fig. 13. We clearly see both the initial transient and the final travelling wave solution. For comparison purposes, the same computation was performed using the finite difference comparison scheme for the effective equation. Fig. 14 shows the errors of the patch dynamics simulation with respect to the finite difference simulation. We see that during the transient phase the error oscillates somewhat, but once the travelling wave is steady the error increases linearly, due to a difference in the approximated propagation speed. Note that the error is significantly larger than for example 5.1, due to the fact that the estimator is less accurate, but also because the macroscopic time-step is much smaller, resulting in a larger number of estimations.

6. Conclusions

We described the patch dynamics scheme for multi-scale problems. This scheme approximates an unavailable *effective* equation over macroscopic time and length scales, when only a microscopic evolution law is given; it only uses appropriately initialized simulations of the microscopic model over small subsets (patches) of the space-time domain. Because it is often not possible to impose macroscopically inspired boundary conditions on a microscopic simulation, we propose to use buffer regions around the patches, which temporarily shield the internal region of the patches from boundary artefacts.

We analytically derived an error estimate for a model homogenization problem with Dirichlet boundary conditions. The numerical results show that the algorithm is more widely applicable. We showed the scheme is capable of giving good approximations for reaction–diffusion systems, as well as for fourth-order PDEs, such as the Kuramoto–Sivashinsky equation. As such, these results are far more general than those of [35], which are restricted to reaction–diffusion problems due to the special choice of boundary conditions.

We emphasize that, although analyzed for homogenization problems, the real advantage for the methods presented here lies in their applicability for microscopic models that are not PDEs, such as kinetic Monte-Carlo, or molecular dynamics. Experiments in this direction are currently being pursued actively.

Acknowledgments

Giovanni Samaey is a Research Assistant of the Fund for Scientific Research – Flanders. This work has been partially supported by Grant IUAP/V/22 and by the Fund of Scientific Research through Research Project G.0130.03 (G.S. and D.R.), and an NSF/ITR Grant and AFOSR Dynamics and Control, Dr. S. Heise (IGK).

References

[1] A. Abdulle, W. E, Finite difference heterogeneous multi-scale method for homogenization problems, J. Comput. Phys. 191 (1) (2003) 18–39.
[2] G. Allaire, Homogenization and two-scale convergence, SIAM J. Math. Anal. 23 (6) (1992) 1482–1518.
[3] I. Babuska, Homogenization and its applications, in: B. Hubbard (Ed.), SYNSPADE, 1975, pp. 89–116.
[4] M. Bär, Räumliche Strukturbildung bei einer Oberflächenreaktion. Chemische Wellen und Turbulenz in der CO-Oxidation auf Platin-Einkristal-oberflächen, Ph.D. Thesis, Freie Universität Berlin, 1993.
[5] M. Bär, A. Bangia, I. Kevrekidis, G. Haas, H.-H. Rotermund, G. Ertl, Composite catalyst surfaces: effect of inert and active heterogeneities on pattern formation, J. Phys. Chem. 100 (1996) 19106–19117.
[6] A. Bensoussan, J. Lions, G. Papanicolaou, Asymptotic Analysis of Periodic Structures: Studies in Mathematics and its Applications, vol. 5, North Holland, Amsterdam, 1978.
[7] D. Cioranescu, P. Donato, An Introduction to Homogenization, Oxford University Press, Oxford, 1999.
[8] M. Dorobantu, B. Engquist, Wavelet-based numerical homogenization, SIAM J. Numer. Anal. 35 (2) (1998) 540–559.
[9] W. E, B. Engquist, The heterogeneous multi-scale methods, Comm. Math. Sci. 1 (1) (2003) 87–132.
[10] J. Elezgaray, G. Berkooz, P. Holmes, Large-scale statistics of the Kuramoto–Sivashinsky equation: a wavelet-based approach, Phys. Rev. E 54 (1996) 224–230.
[11] B. Engquist, Computation of oscillatory solutions to hyperbolic differential equations, Springer Lecture Notes Math. 1270 (1987) 10–22.
[12] B. Engquist, O. Runborg, Wavelet-based numerical homogenization with applications, in: Multiscale and Multiresolution Methods: Lecture Notes in Computational Science and Engineering, vol. 20, Springer, Berlin, 2002, pp. 97–148.
[13] C. Gear, I. Kevrekidis, Projective methods for stiff differential equations: problems with gaps in their eigenvalue spectrum, SIAM J. Sci. Comput. 24 (4) (2003) 1091–1106, can be obtained as NEC Report 2001-029, http://www.neci.nj.nec.com/homepages/cwg/projective.pdf.
[14] C.W. Gear, I.G. Kevrekidis, A legacy-code approach to low-dimensional computation: constraint-defined manifolds, J. Sci. Comp. 25 (1) (2006), in press.
[15] C. Gear, J. Li, I. Kevrekidis, The gap-tooth method in particle simulations, Phys. Lett. A 316 (2003) 190–195, can be obtained as cond-mat/0211455 at arxiv.org.
[16] M. Graham, I. Kevrekidis, K. Asakura, J. Lauterbach, K. Krischer, H.-H. Rotermund, G. Ertl, Effects of boundaries on pattern formation: catalytic oxidation of CO on Platinum, Science 264 (1994) 80–82.
[17] N. Hadjiconstantinou, Hybrid atomistic-continuum formulations and the moving contact-line problem, J. Comput. Phys. 154 (1999) 245–265.
[18] A.C. Hindmarsh, ODEPACK, A Systematized Collection of ODE Solvers, in: R.S. Stepleman et al. (Eds.), Scientific Computing, North-Holland, Amsterdam, 1983, pp. 55–64.

[19] T. Hou, X. Wu, A multiscale finite element method for elliptic problems in composite materials and porous media, J. Comput. Phys. 134 (1997) 169–189.
[20] T. Hou, X. Wu, Convergence of a multiscale finite element method for elliptic problems with rapidly oscillating coefficients, Math. Comput. 68 (227) (1999) 913–943.
[21] G. Hummer, I. Kevrekidis, Coarse molecular dynamics of a peptide fragment: free energy, kinetics and long-time dynamics computations, J. Chem. Phys. 118 (23) (2003) 10762–10773, can be obtained as physics/0212108 at arxiv.org.
[22] E. Jones, T. Oliphant, P. Peterson, et al., SciPy: Open source scientific tools for Python (2001). Available from: <http://www.scipy.org/>.
[23] J. Keener, Homogenization and propagation in the bistable equation, Physica D 136 (2000) 1–17.
[24] I. Kevrekidis, Coarse bifurcation studies of alternative microscopic/hybrid simulators, Plenary lecture, CAST Division, AIChE Annual Meeting, Los Angeles, 2000, slides can be obtained from: <http://arnold.princeton.edu/~yannis/>.
[25] I. Kevrekidis, C. Gear, J. Hyman, P. Kevrekidis, O. Runborg, C. Theodoropoulos, Equation-free multiscale computation: enabling microscopic simulators to perform system-level tasks, Comm. Math. Sci. 1 (4) (2003) 715–762.
[26] I. Kevrekidis, B. Nicolaenko, J. Scovel, Back in the saddle again: a computer assisted study of the Kuramoto–Sivashinsky equation, SIAM J. Appl. Math. 50 (1990) 760–790.
[27] J. Li, P. Kevrekidis, C. Gear, I. Kevrekidis, Deciding the nature of the ''coarse equation'' through microscopic simulations: the baby-bathwater scheme, SIAM Multiscale Model. Simul. 1 (3) (2003) 391–407.
[28] J. Li, D. Liao, S. Yip, Imposing field boundary conditions in MD simulation of fluids: optimal particle controller and buffer zone feedback, Mat. Res. Soc. Symp. Proc. 538 (1998) 473–478.
[29] A. Makeev, D. Maroudas, I. Kevrekidis, Coarse stability and bifurcation analysis using stochastic simulators: kinetic Monte Carlo examples, J. Chem. Phys. 116 (2002) 10083–10091.
[30] A. Makeev, D. Maroudas, A. Panagiotopoulos, I. Kevrekidis, Coarse bifurcation analysis of kinetic Monte Carlo simulations: a lattice-gas model with lateral interactions, J. Chem. Phys. 117 (18) (2002) 8229–8240.
[31] A. Matache, I. Babuska, C. Schwab, Generalized p-FEM in homogenization, Numerische Mathematik 86 (2) (2000) 319–375.
[32] N. Neuss, W. Jäger, G. Wittum, Homogenization and multigrid, Computing 66 (1) (2001) 1–26.
[33] O. Runborg, C. Theodoropoulos, I. Kevrekidis, Effective bifurcation analysis: a time-stepper based approach, Nonlinearity 15 (2002) 491–511.
[34] G. Samaey, I. Kevrekidis, D. Roose, Damping factors for the gap-tooth scheme, in: S. Attinger, P. Koumoutsakos (Eds.), Multiscale Modelling and Simulation, Lecture Notes in Computational Science and Engineering, vol. 36, Springer, Berlin, 2004, pp. 93–102.
[35] G. Samaey, D. Roose, I. Kevrekidis, The gap-tooth scheme for homogenization problems, SIAM Multiscale Model. Simul. 4 (1) (2005) 278–306.
[36] C. Schwab, A. Matache, Multiscale and Multiresolution Methods: Lecture Notes in Computational Science and Engineering, vol. 20, Springer-Verlag, New York, 2002, pp. 197–238, Ch. Generalized FEM for homogenization problems.
[37] S. Setayeshar, C. Gear, H. Othmer, I. Kevrekidis, Application of coarse integration to bacterial chemotaxis, SIAM Multiscale Model. Simul. 4 (1) (2005) 307–327.
[38] C. Siettos, A. Armaou, A. Makeev, I. Kevrekidis, Microscopic/stochastic timesteppers and coarse control: a kinetic Monte Carlo example, AIChE J. 49 (7) (2003) 1922–1926, can be obtained as nlin.CG/0207017 at arxiv.org.
[39] C. Siettos, M. Graham, I. Kevrekidis, Coarse Brownian dynamics for nematic liquid crystals: bifurcation, projective integration and control via stochastic simulation, J. Chem. Phys. 118 (22) (2003) 10149–10157, can be obtained as cond-mat/0211455 at arxiv.org.
[40] S. Shvartsman, E. Schütz, R. Imbihl, I. Kevrekidis, Dynamics on microcomposite catalytic surfaces: the effect of active boundaries, Phys. Rev. Lett. 83 (1999) 2857–2860.
[41] C. Theodoropoulos, Y. Qian, I. Kevrekidis, Coarse stability and bifurcation analysis using time-steppers: a reaction–diffusion example, in: Proceedings of the National Academy of Sciences USA, vol. 97, 2000.
[42] C. Theodoropoulos, K. Sankaranarayanan, S. Sundaresan, I. Kevrekidis, Coarse bifurcation studies of bubble flow Lattice-Boltzmann simulations, Chem. Eng. Sci. 59 (2003) 2357–2362, can be obtained as nlin.PS/0111040 from arxiv.org.
[43] P. Van Leemput, K. Lust, I.G. Kevrekidis, Coarse-grained numerical bifurcation analysis of lattice Boltzmann models, Physica D: Nonlinear Phenomena, 210 (1–2) (2005) 58–76.